

**Supporting Information**

**Zinc Blende Inspired Rational Design of  $\beta$ -SiC Based  
Resilient Anode Material for Lithium-Ion Batteries**

Ravi Nandan,<sup>a</sup> Noriyuki Takamori,<sup>a</sup> Koichi Higashimine,<sup>b</sup> Rajashekar Badam,<sup>a</sup> Noriyoshi

Matsumi<sup>a,\*</sup>

<sup>a</sup>Graduate School of Advanced Science and Technology,

Japan Advanced Institute of Science and Technology,

<sup>b</sup>Center for Nano Materials and Technology,

Japan Advanced Institute of Science and Technology,

\*E-mail: - [matsumi@jaist.ac.jp](mailto:matsumi@jaist.ac.jp) (Prof. Noriyoshi Matsumi)

Tel: +81-761-51-1600

## **Experimental Methods**

### **Materials**

(3-Aminopropyl)triethoxysilane (APTES, 99%), Sodium carboxymethyl cellulose(CMC, average MW~250000) and Poly(acrylic acid)(PAA) were purchased from Sigma-Aldrich. 1.0 M Tris-HCl (pH 8.5) was purchased from Nippon Gene. Melamine Monomer (>98%), Sodium L-ascorbate (>98%), and 3-Hydroxytyramine Hydrochloride (>98%) were procured from TCI Co., Ltd. Acetylene Black (AB) from Denka Japan Private Co., Ltd was adopted as the conductive material. The thickness of Cu foil (used as the current collector) is ~ 20  $\mu\text{m}$ . It was obtained from the Nilaco corporation. All chemicals were used as received.

### **Materials Synthesis**

The complete synthesis process of  $\beta$ -SiC nanoparticles embedded carbon matrix can be easily understand with the help of following small steps which is also pictorially represented in Figure 1 (main text).

A: - A solution of 3-(Aminopropyl)triethoxysilane (APTES), methanol and water was kept for stirring at 1000 rpm for 30 min.

B: - Addition of L-Ascorbic acid solution to obtain water dispersible Si nanoparticles (Figure S1).<sup>1</sup>

C: - Introduction of dopamine (hydroxytyramine hydrochloride) in water dispersed Si nanoparticle solution, as prepared in part “B”. Followed by addition of TRIS-8.5 pH buffer solution to effect polymerization of dopamine to polydopamine.<sup>2</sup>

D: - To tune nitrogen content we introduced melamine ( $C_3H_6N_6$ , nitrogen ~ 75 % by wt.) in the solution obtained in part C.

E: - The complete solution (Si nanoparticle coated polydopamine + melamine) allowed to stir (@500 rpm) over night to obtain a good homogeneity.

F: - The powder (melamine-poydopamine-Si matrix) obtained after centrifuging and freeze drying was collected and crushed using mortar-pestle to obtain the final powder.

G:- The final powder obtained in part “F” was subjected to pyrolysis in nitrogen ambiance as shown in Figure S2. In this study, two pyrolysis temperature of 600 and 1050 °C were used and subsequently samples were named as MAD600 and

MAD1050. Where M stands for melamine, A for APTES, D for dopamine and 600 and 1050 are respective pyrolysis temperatures.

### **Characterization**

The thermogravimetric analysis (TGA) was carried out using STA 7200 Thermal Analysis System from HITACHI. The X-ray photoelectron spectroscopic (XPS) studies were carried out using S-Probe Surface Spectrometer. The transmission electron microscopic (TEM) studies were carried out using Hitachi HF-2000. For the electrochemical testing the standard battery fabrication process was followed. For cell assembly MBRAUN LABSTAR glove box facility maintained in argon environment is used. The electrochemical studies were carried out using BSC-805, Bio Logic Science Instrument station.

For elemental atomic percentage calculation using XPS spectra following procedure was followed. The nitrogen atomic percentage in MAD600, MAD1050 and MD samples were determined by integrating the area under the curves of respective XPS spectrum. The calculated area under curves were normalized with their respective sensitivity factor (SF, equation 1).<sup>3,4</sup>

$$\text{At. \%} = \frac{\frac{A_m}{SF_m}}{\sum_m \frac{A_m}{SF_m}} * 100 \quad (\text{S1})$$

Where,

m = C /N/O/Si

SF<sub>C</sub> = 0.25; SF<sub>N</sub> = 0.42; SF<sub>O</sub> = 0.66 and SF<sub>Si</sub> = 0.27

### **Slurry Preparation**

The slurry of the respective anode materials (MAD600/1050, Si30 nm, SiC, SiC@C600, MD) for making of working electrode were prepared using ball-milling facility (FRITSCH – Premium line, Pulverisette 7). The slurry composition for this study was maintained as *Active material : AB : PAA : CMC :: 70 : 15 : 7.5 : 7.5* by weight. The deionized water was used as the solvent. The obtained slurry was coated on the battery grade Cu foil as the current collector using doctor blade and kept under vacuum at 80 °C for overnight prior to standard roll pressing.

### **Cell assembly**

The working electrodes were punched for study with CR2025-coin cells. The counter electrode used was lithium foil for half cells (anodic or cathodic). The

electrolyte used was commercially available 1.0 M LiPF<sub>6</sub> solution mixture of ethylene carbonate (EC) and diethyl carbonate (1:1 by volume). Celgard 2500 polypropylene was used as the separator. In addition, the fabrication of the full cell was proceeded by adopting LiCoO<sub>2</sub> as a counter electrode after pre-cycling treatment. These components were assembled in the gloved box where O<sub>2</sub> and H<sub>2</sub>O concentration were below 0.5 ppm. The fabricated cells were kept for 10 h to stabilize before proceeding with the electrochemical measurements.

### **Full-cell assembly**

In order to minimize the possible initial irreversible Li<sup>+</sup>-ions loss in full cell, we first assembled the MAD1050 based anodic and LiCoO<sub>2</sub> based cathodic half-cells separately with lithium foil as counter and reference electrode. These cells were cycled for few cycles in their respective half-cell configurations. Following this, they were dismantled to recover the activated LiCoO<sub>2</sub> and MAD1050 electrodes from their respective half-cells. These recovered electrodes were used as cathode and anode, respectively, for assembling the LiCoO<sub>2</sub>//MAD1050 based full-cells. Figure S21 and S22 shows the CV and cyclic study of LiCoO<sub>2</sub> based cathodic half-cells with Li-foil as counter and reference electrode. The CV and cyclic studies

have been used to regulate the operational potential window for charging/discharging and optimum anode material (MAD1050) loading, in full cell.<sup>5</sup> The optical photograph (Figure S23) of one of the assembled full cells (LiCoO<sub>2</sub>//MAD1050) shows an open circuit voltage (OCV) of ~3.2 V.

The loading of anode electrode was optimized in light to the equation S2.<sup>6</sup>

$$\frac{C_A \cdot m_A}{C_C \cdot m_C} \geq 1 \quad (\text{S2})$$

Where,

$C_A / C_C$  → Specific capacity of anode / cathode, respectively,

$m_A / m_C$  → Mass loading of anode / cathode, respectively.

### **Post cyclic (*ex-situ*) studies**

A coin cell in anodic configuration with MAD1050 as anode material was subjected to the cycling study at a charge/discharge current of 100 mA/g, following, 200 cycles of lithiation-delithiation the coin cell was carefully dismantled in argon filled glove box. The recovered anode electrode (i.e. MAD1050 film on Cu foil) was carefully transferred from glove box to XPS and SEM facilities for recording the spectrum and imaging, respectively.

**Table S1.** Circuit parameters corresponding to Si30nm and MAD1050 Nyquist plots

(Figure 5c in main text)

<b>Resistance (<math>\Omega</math>)</b>	<b>Si</b>	<b>MAD1050</b>
$R_{sol}$ (solution resistance)	2.248	6.322
$R_{sf}$ (SEI resistance)	50.76	35.5
$R_{ct}$ (Charge transfer resistance)	9.637	9.176



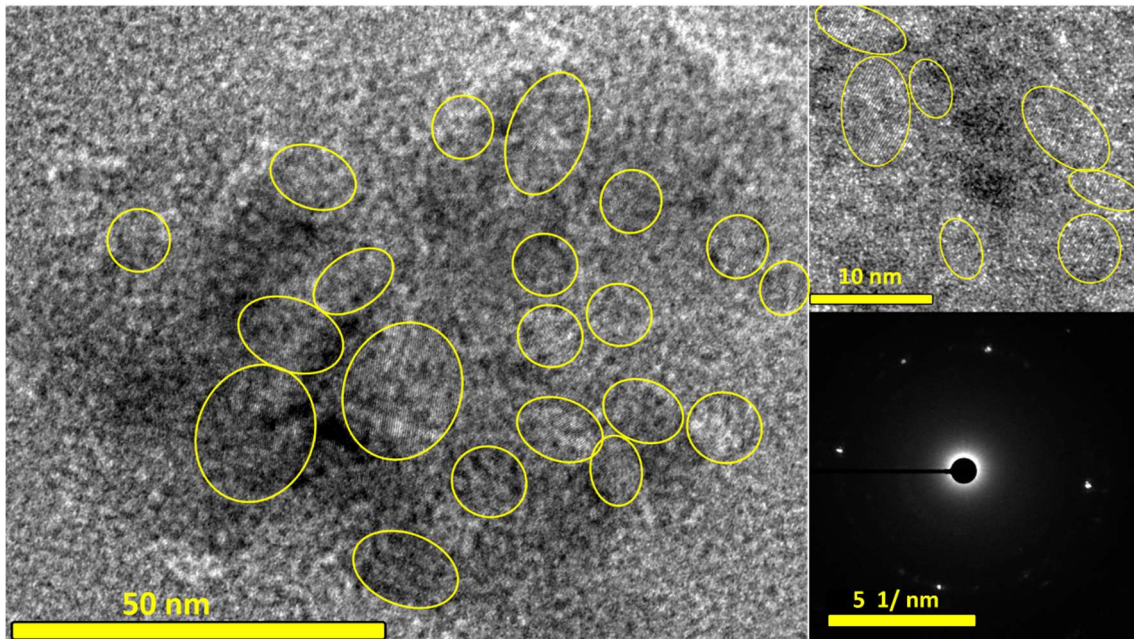


**Figure S1.** (a,b) High-resolution transmission electron microscopic images of Si nanoparticles at different magnifications. (c) The concomitant selected area diffraction pattern.

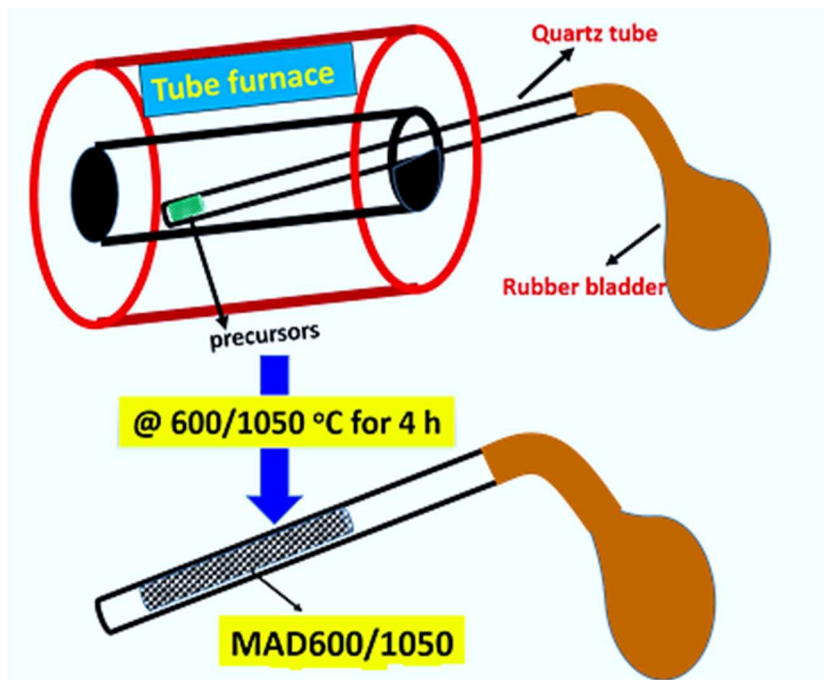


**Figure S2.** Schematic representation of pyrolysis process for MAD600/1050.

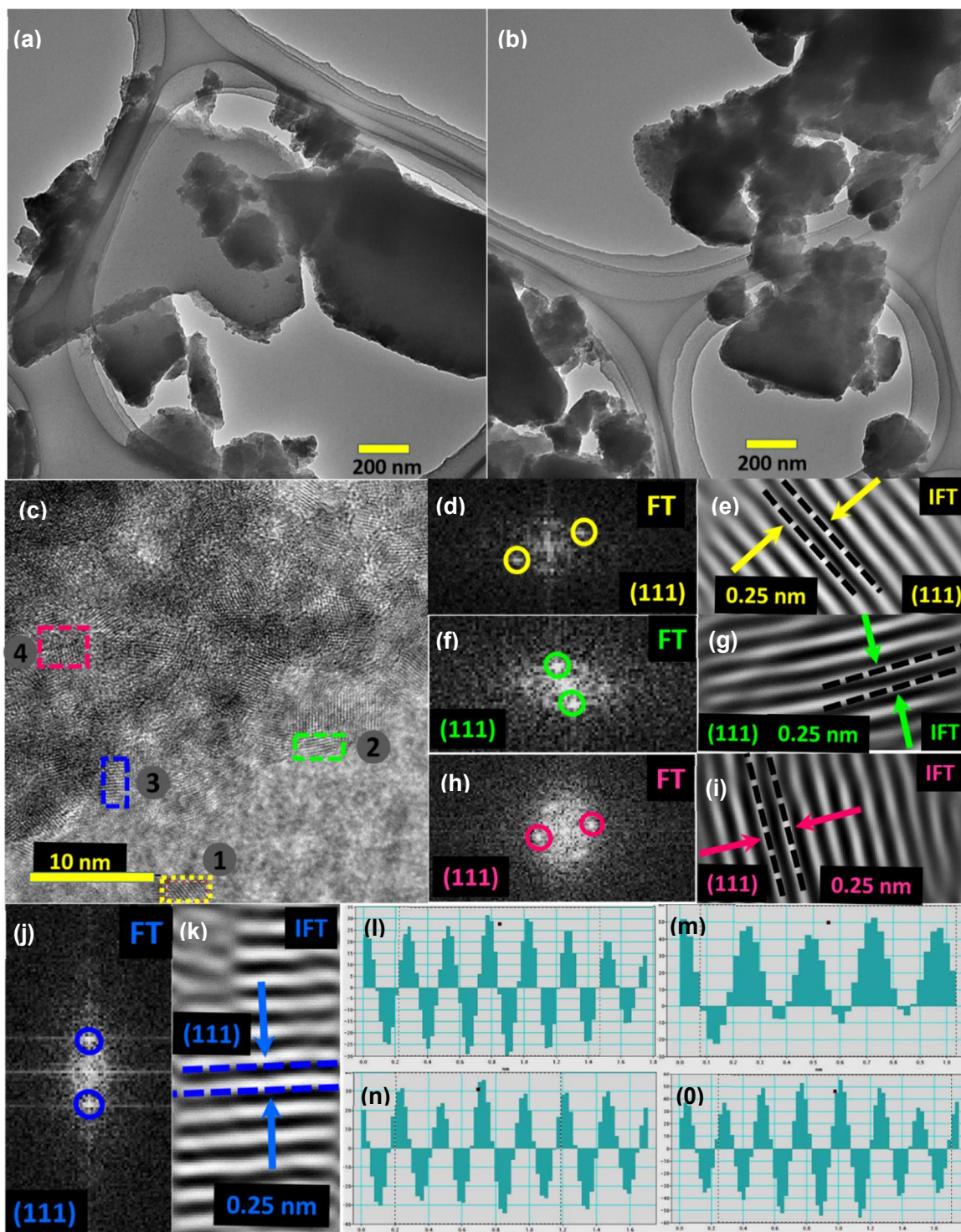


**Figure S3.** (a,b) Representative bright field transmission electron microscopic (TEM) images and (c) high resolution (HR) TEM (HRTEM) image of MAD600. Boxes 1-4 indicate the HRTEM images of randomly selected  $\beta$ -SiC nanoparticles subjected to

interplanar spacing estimation, (d,e), (f,g), (h,i) and (j,k) show the Fourier and inverse Fourier transformation corresponding to the boxes 1-4, respectively. (l-o) The concomitant line profiles for figure e, g, i and k, respectively. The interplanar spacing are evaluated from the respective line profiles of selected nanoparticles indicated from boxes 1-4.

**Discussion (Figure S3):** - Figure S3a,b show the representative bright field transmission electron microscopic (TEM) images of as-synthesized MAD600 sample. In line to our synthesis protocol the as-synthesized material comprises of  $\beta$ -SiC nanoparticles embedded carbon matrix. This carbon matrix ensures the connectivity between the nanoparticles as well as beneficial for overall electronic conductivity of the material. The high resolution TEM (HRTEM) image (Figure S3c) clearly indicate the crystalline nature of the embedded  $\beta$ -SiC nanoparticles. In an attempt to shed some more light on the nature of these crystalline nanoparticles the associated HRTEM images are subjected to Fourier transform (FT) and inverse FT (IFT) in order to generate the corresponding selected area diffraction patterns (SAED) as well as the associated crystal planes for interplanar spacing determination (Figure S3c-o).

We randomly selected a batch of four nanoparticles (as indicated by 4 colored boxes in Figure S3c) from HRTEM image of MAD600 and subjected to FT and IFT studies. Figure (d,e), (f,g), (h,i) and (j,k) show the respective SAED patterns and concomitant crystal planes associated with these patterns which comprises the nanoparticles marked in boxes 1-4 (Figure S3c). The interplanar spacing calculated from the respective line profiles (l-o) deduced from Figure S3 e, g, i and k, indicate that the nanoparticles are comprise of (111) planes with a characteristic interplanar spacing of 0.25 nm of  $\beta$ -SiC phase. The studies indicates that these  $\beta$ -SiC nanoparticles are mainly comprises of (111) planes with

a characteristic interplanar spacing of 0.25 nm.

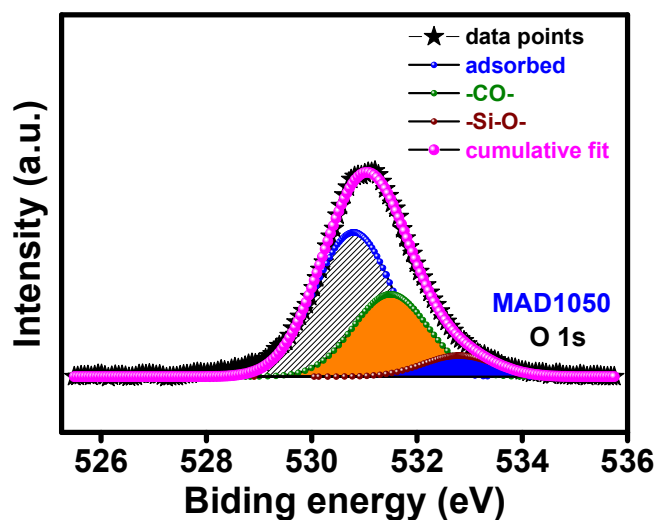


Figure S4. Deconvoluted high resolution XPS spectrum of O1s for MAD1050.

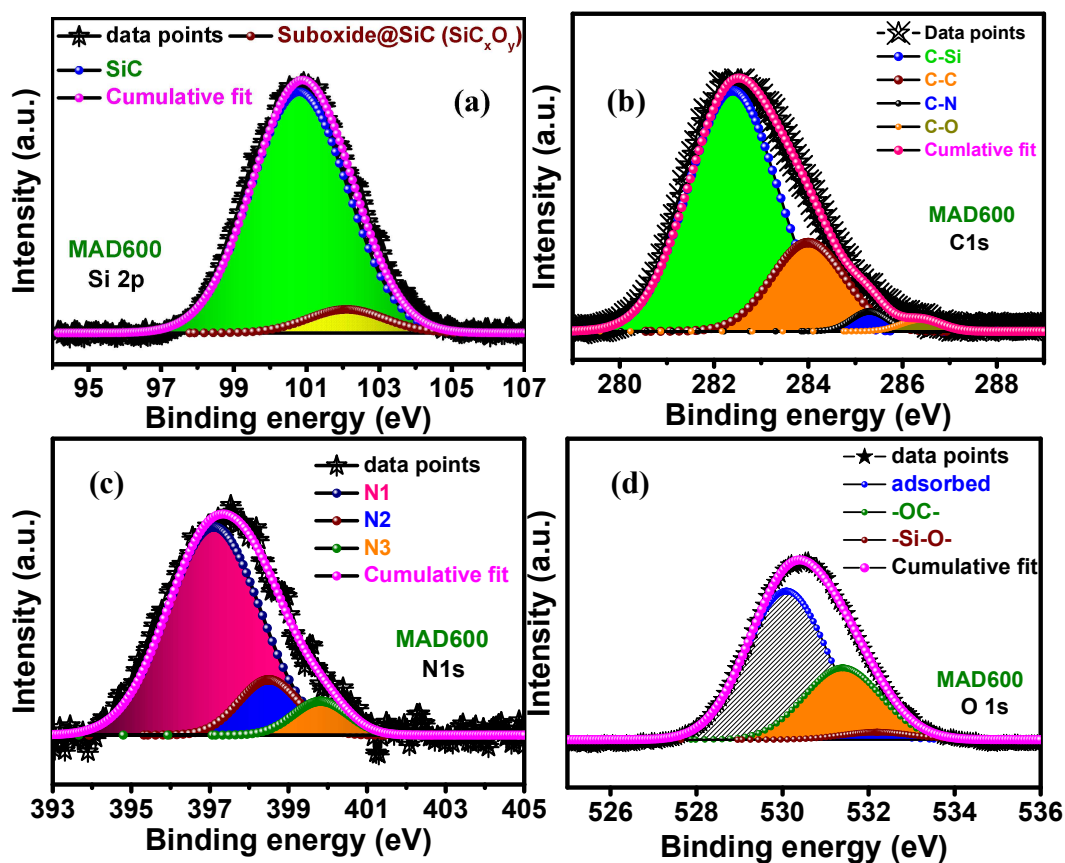
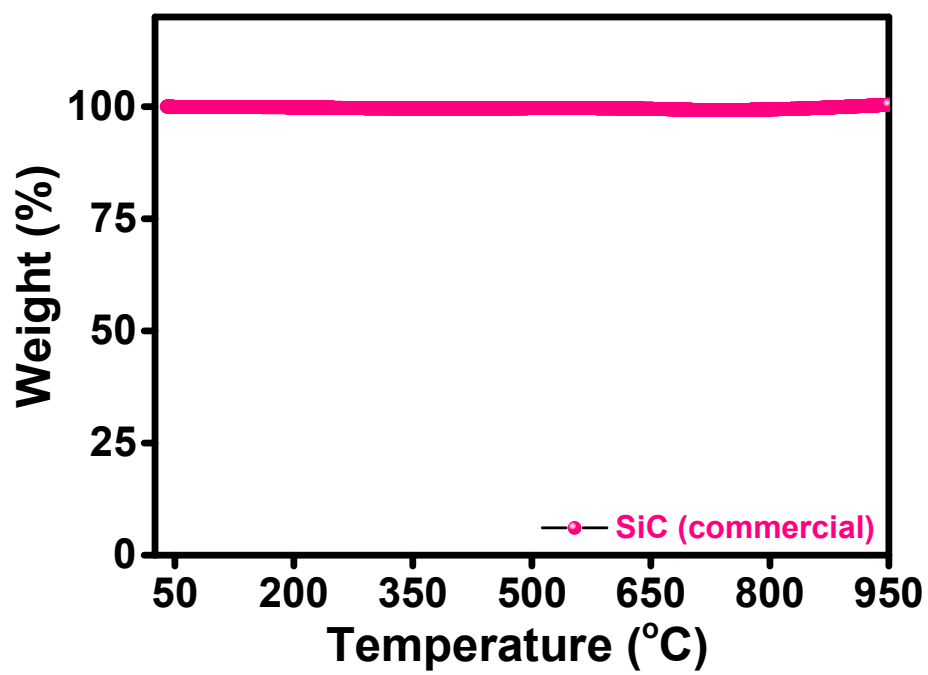
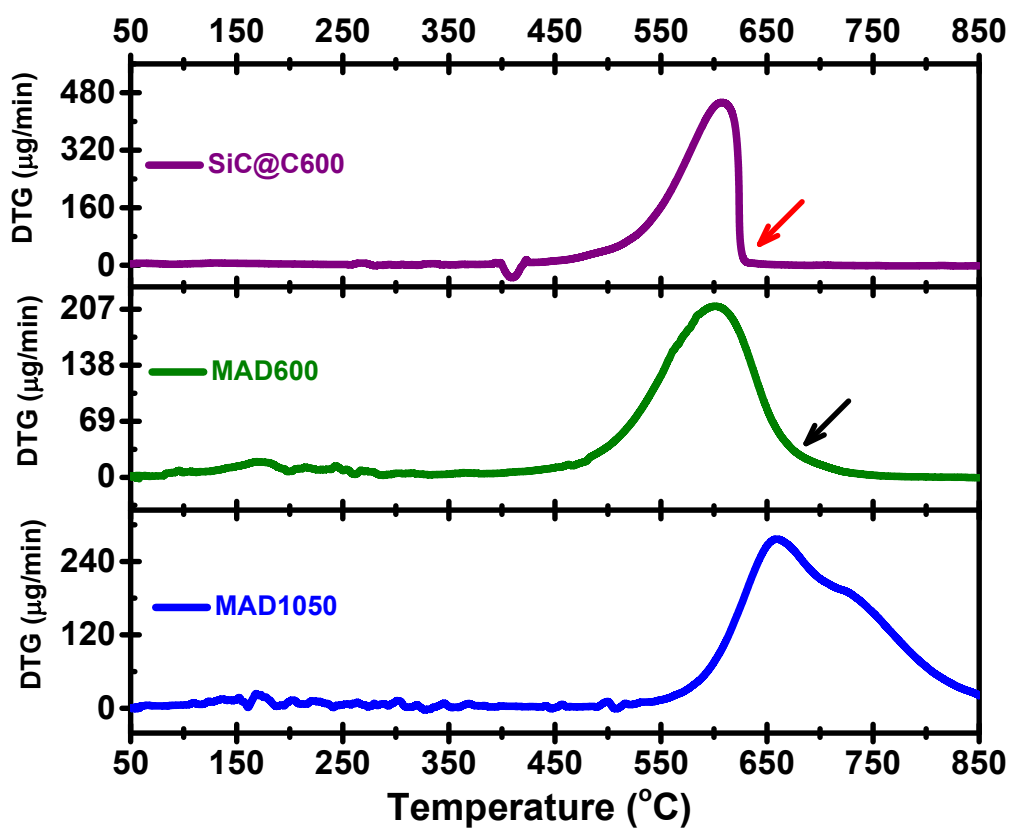


Figure S5. Deconvoluted high resolution XPS spectra of (a) Si2p, (b) C1s, (c) N1s and (d) O1s for MAD600.



**Figure S6.** Thermogravimetric profile of commercial SiC in oxygen ambiance.



**Figure S7.** The DTG profiles for SiC@C600, MAD600 and MAD1050 in oxygen ambience, associated with the TGA profiles as shown in Figure 4a in main text.

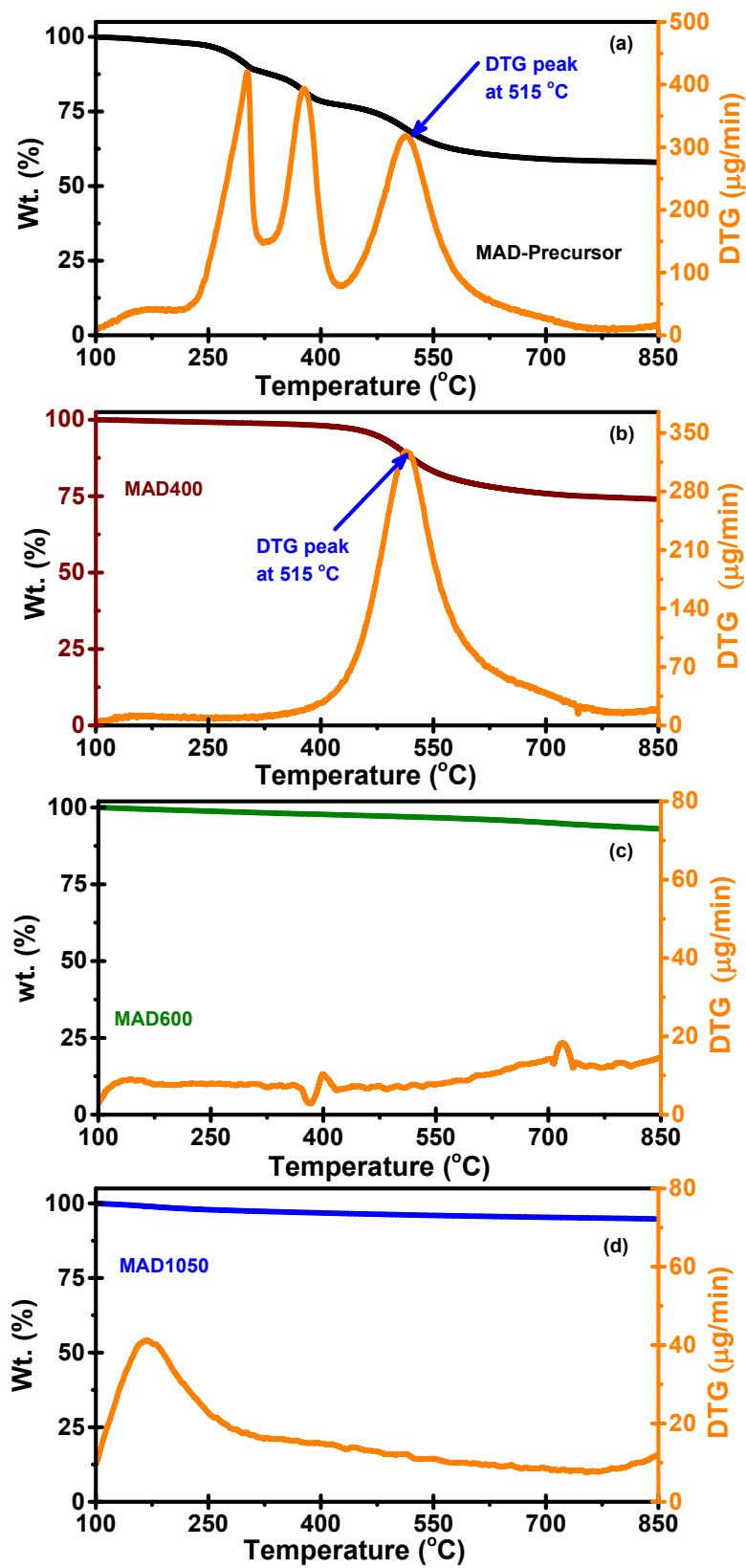


Figure S8. The TGA and concomitant DTG profiles for (a) MAD precursor, (b) MAD400,

(c) MAD600 and (d) MAD1050 in nitrogen ambiance.

**Discussion (Figure S8):** - To elucidate the selection of 600 °C as a possible lower pyrolysis cutoff temperature in the present study, we carried out the thermogravimetric studies on MAD precursor in nitrogen ambiance. The associated TGA and DTG curves for MAD precursor are shown in Figure S8a. The DTG curve unveils that the synthesis of desired material (i.e.  $\beta$ -SiC embedded carbon matrix) in present study is a combination of three successive processes taking place at  $\sim$  300, 375 and 515 °C (Figure S8a). Accordingly, we selected the possible lower pyrolysis temperature as 600 °C. This is further evident by the fact that when the sample synthesized at 400 °C i.e. MAD400, subjected to TGA study in nitrogen ambiance (Figure S8b) shows a process resemblance to that present in the case of MAD precursor at  $\sim$  515 °C (indicated by arrows in DTG curves of MAD precursor and MAD400, Figure S8 a,b). This infers that in the case of MAD400, the targeted material synthesis is incomplete. Interestingly, we did not observe such feature when MAD600 and MAD1050 are subjected to the TGA study in similar nitrogen ambiance (Figure S8 c,d).



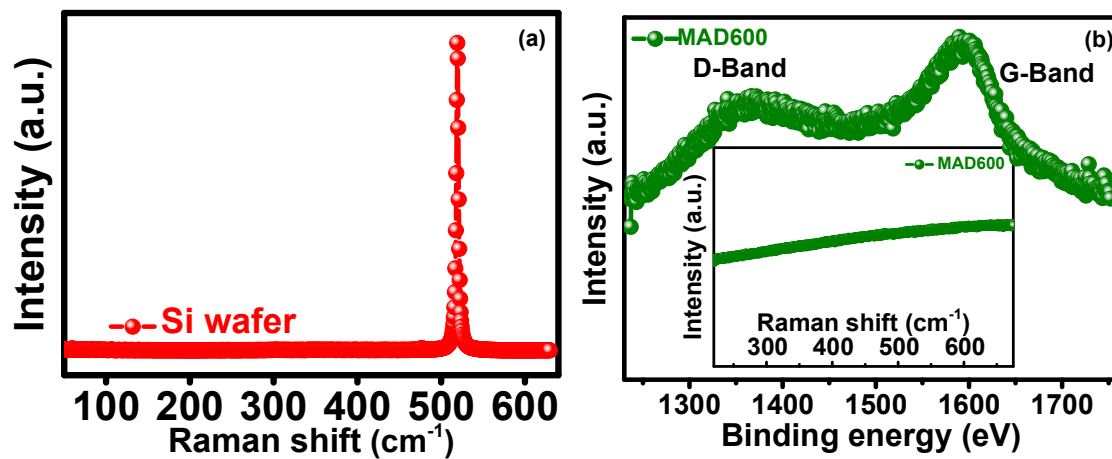


Figure S9. Raman spectra on (a) commercial Si wafer and (b) MAD600 sample.

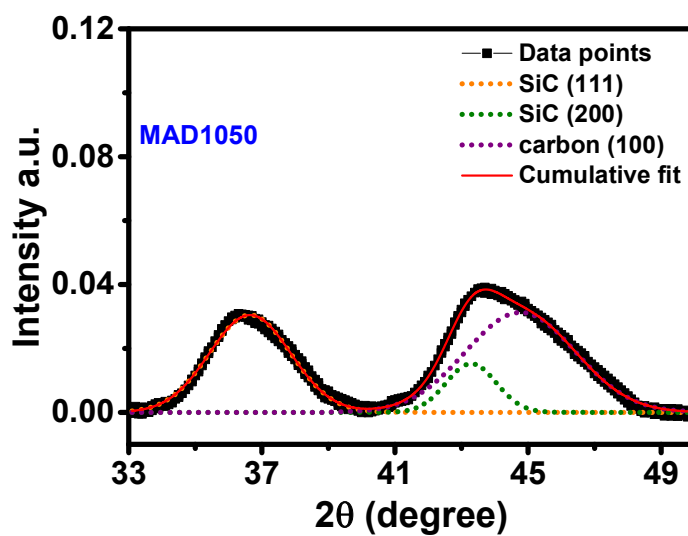


Figure S10. The selected portion of XRD pattern of MAD1050 in 33-50° (from Figure 4c in main text).

### **$\beta$ -SiC nanoparticles size estimation using Scherrer equation**

The particle size (S) is estimated from XRD (Figure S10) using Scherrer formula<sup>7</sup>

$$S = \frac{K \lambda}{FWHM * \cos\theta}$$

(S3)

Where

K= 0.89,

$\lambda$ = 0.15406 nm,

FWHM = full width at half maximum,

$\theta$  is in radian.

The FWHM values for (111) and (200) set of peaks for  $\beta$ -SiC were  $\sim 2.9^\circ$  and  $1.8^\circ$  (Figure S10), respectively. The estimated average particle size was found to be  $\sim 4$  nm, which is consistent with TEM study ( $\sim 5$ nm).

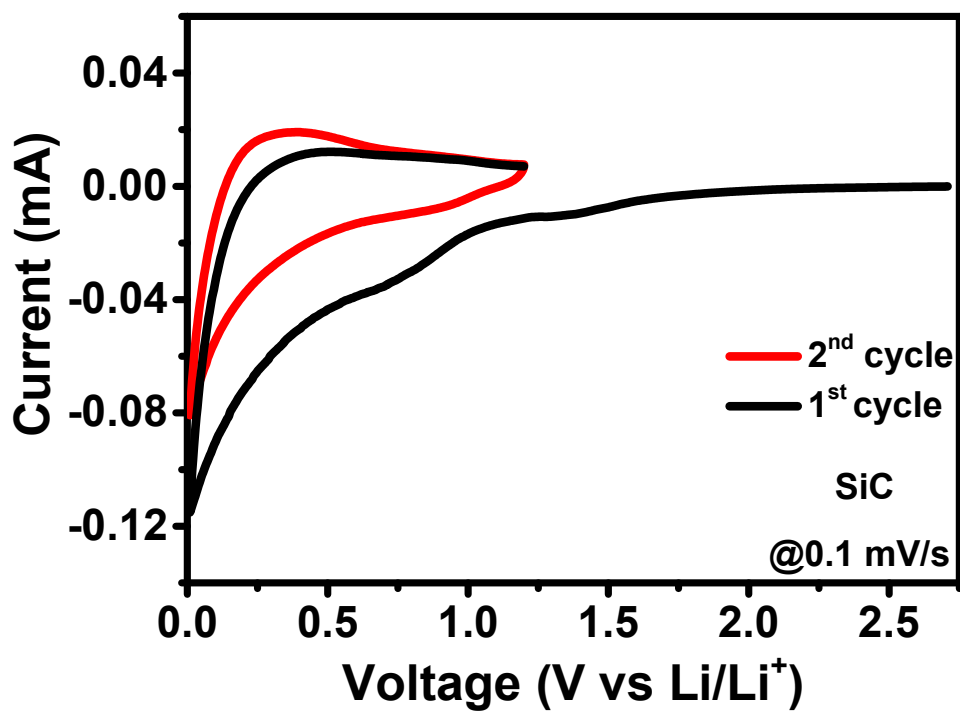
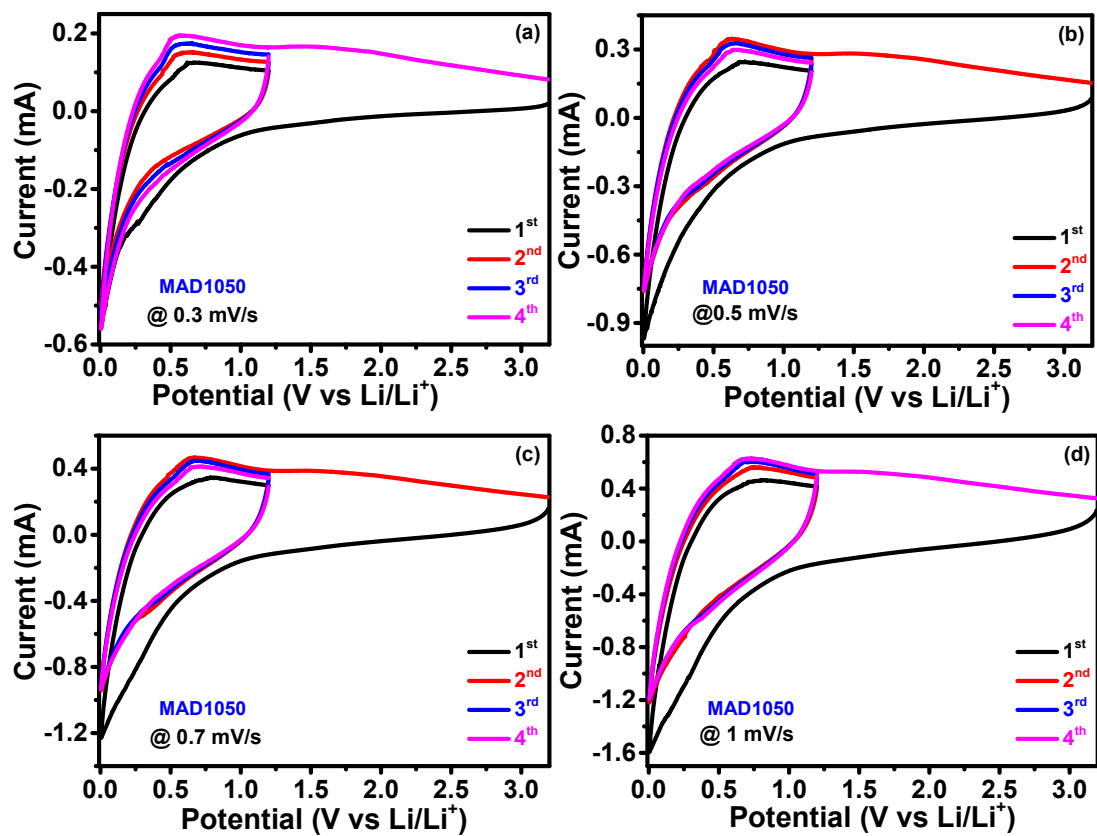
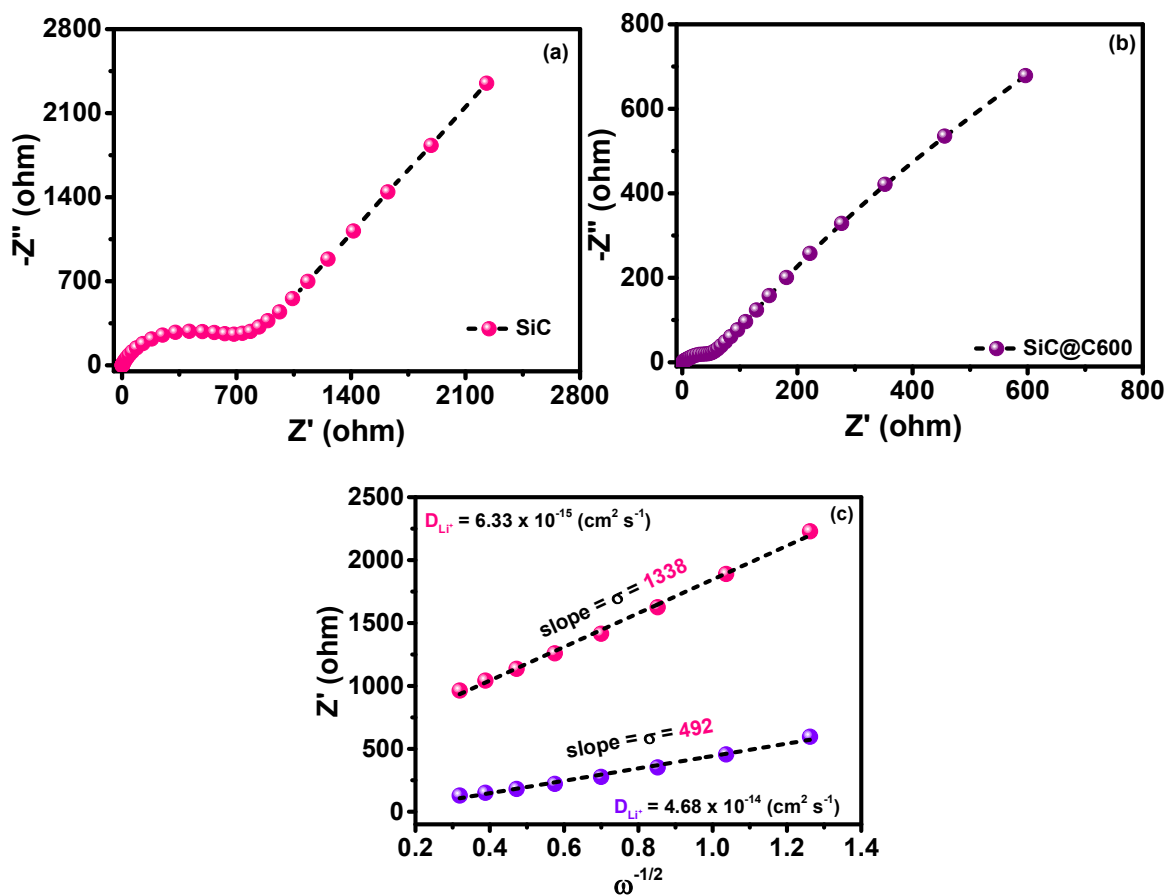


Figure S11. Cyclic voltammograms (CV) on commercial SiC based anodic half-cell.



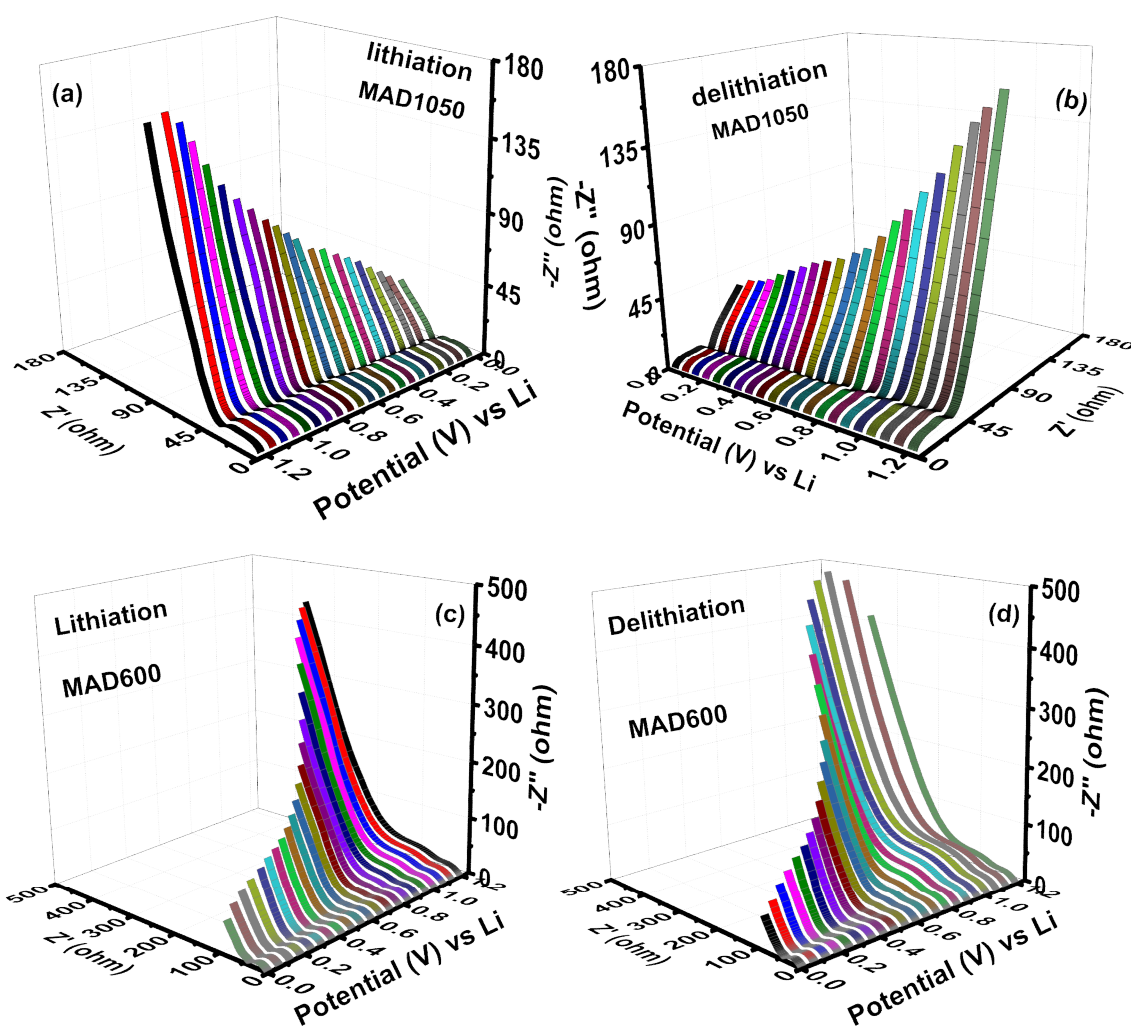
**Figure S12.** Cyclic voltammograms (CV) on MAD1050 based anodic half-cell at a different potential scan speed of (a) 0.3 mV/s, (b) 0.5 mV/s, (c) 0.7 mV/s and (d) 1 mV/s.



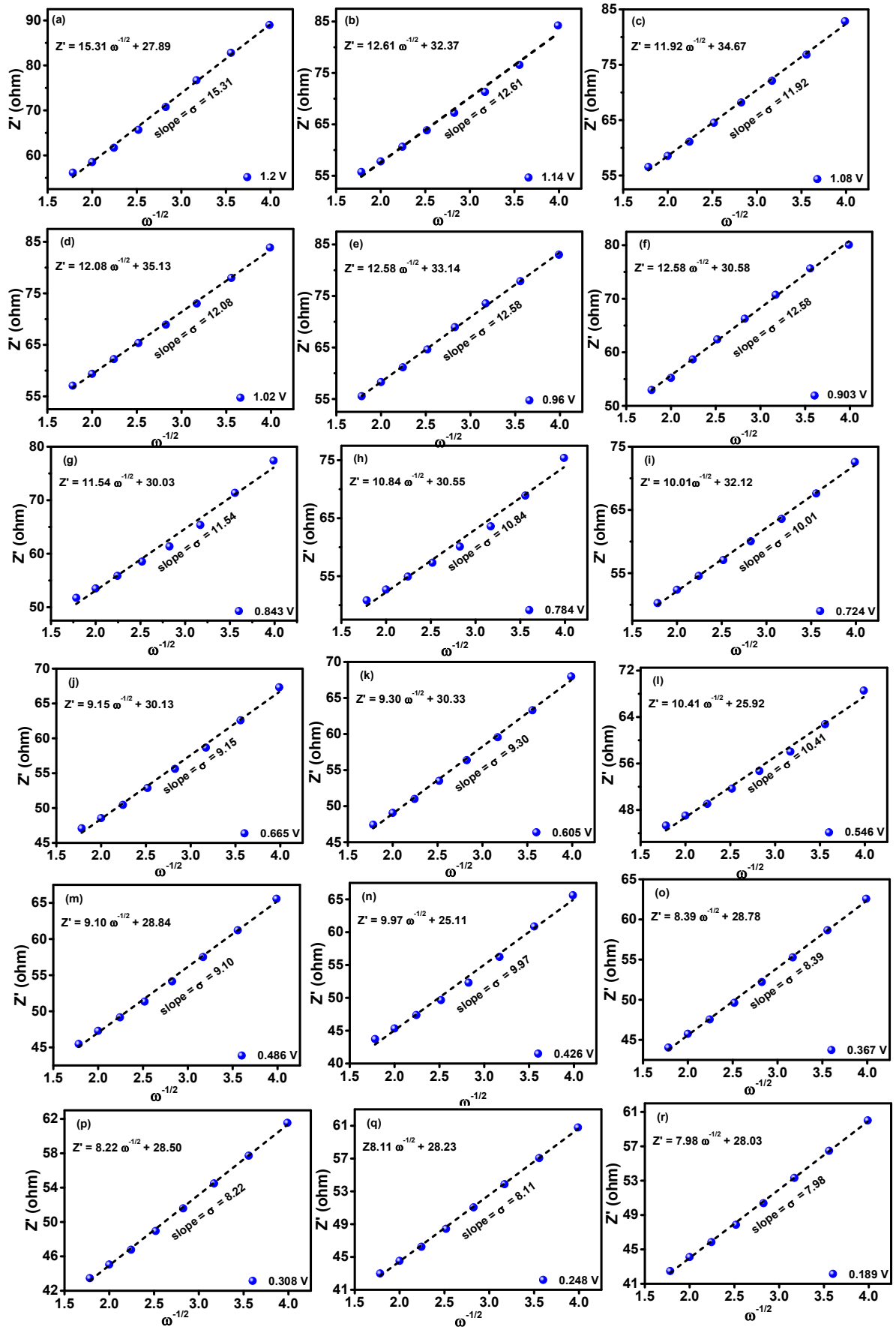
**Figure S13.** Nyquist plots after CV on (a) commercial SiC and (b) SiC@C600 based anodic half-cells. (c) Warburg plots for commercial SiC and SiC@C600 deduced from Figure S13a,b.

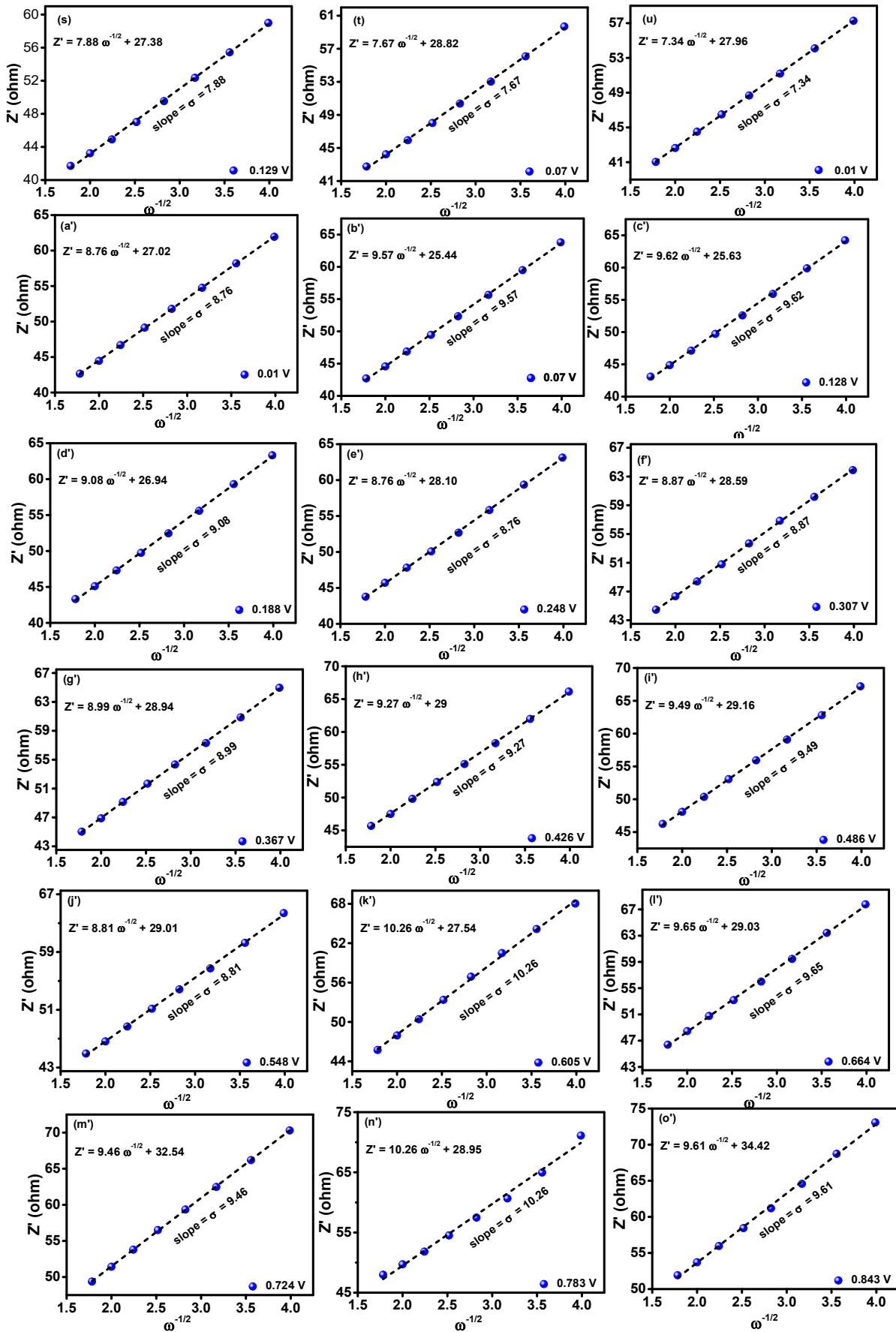
The lithium diffusion coefficients for SiC and SiC@C600, as shown in Figure S13c, were estimated using equation 1 and 2 (from main text) and the respective Warburg coefficients obtained from Figure S13c which are found to be  $4.68 \times 10^{-14} \text{ cm}^2/\text{s}$  and  $6.33 \times 10^{-15} \text{ cm}^2/\text{s}$  for SiC@C600 and SiC, respectively. This indicates that the

surface modification of commercial SiC by means of carbon shell supports the lithium diffusion kinetics and can be attributed to the reduced lithiation surface energy.<sup>8</sup>

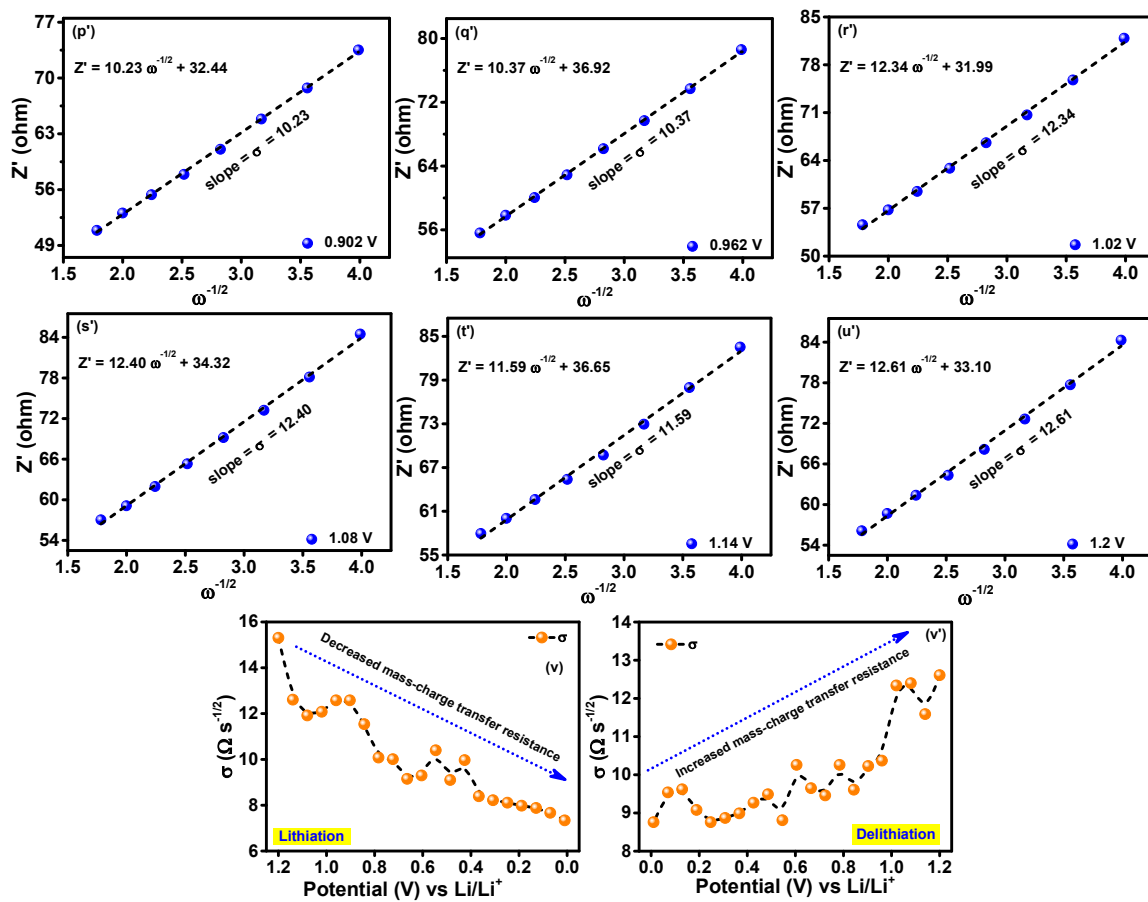


**Figure S14.** DEIS profiles for lithiation and delithiation potential windows on (a,b) MAD1050 and (c,d) MAD600 anode post 300 cyclic study at 50 mA/g of current density.

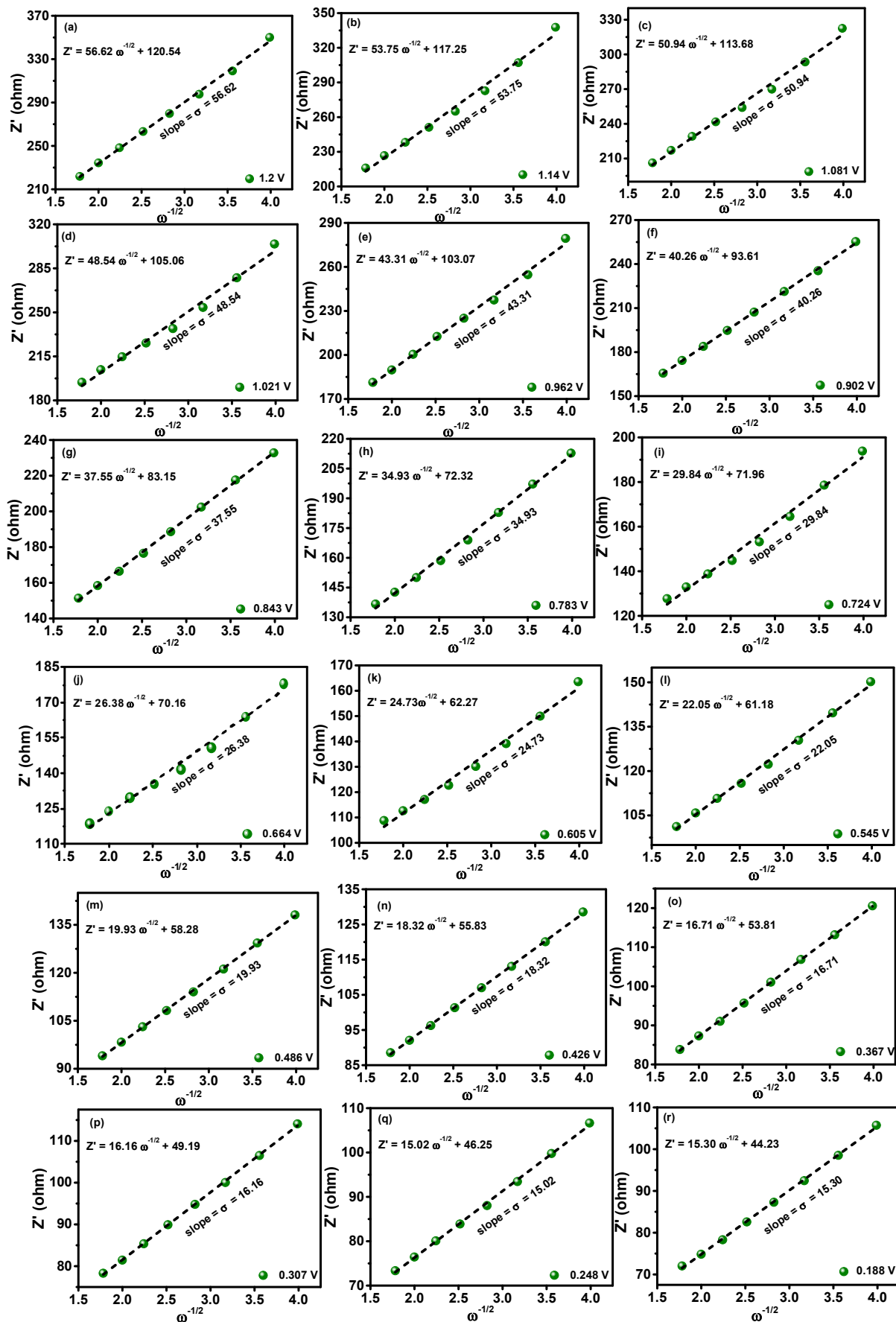


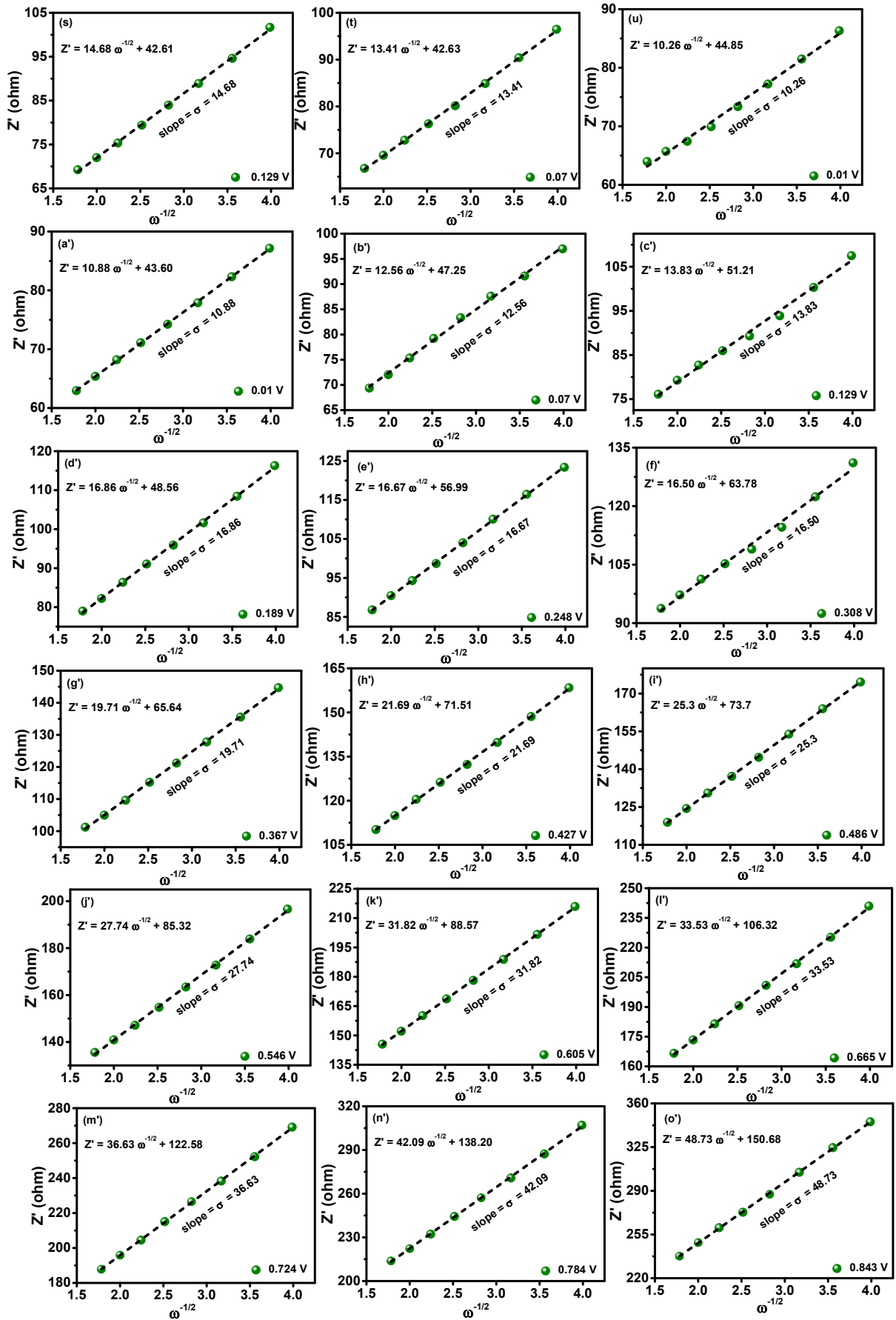






**Figure S15.** Warburg plots, deduced from low frequency portion of DEIS spectra (Figure S14 a, b) on MAD1050 post 300 cyclic study, for lithiation (a-u) and delithiation (a'-u'). Variation of Warburg coefficient with respect to the potential associated with lithiation (V) and delithiation (V') which were obtained from slope of respective Warburg plots.





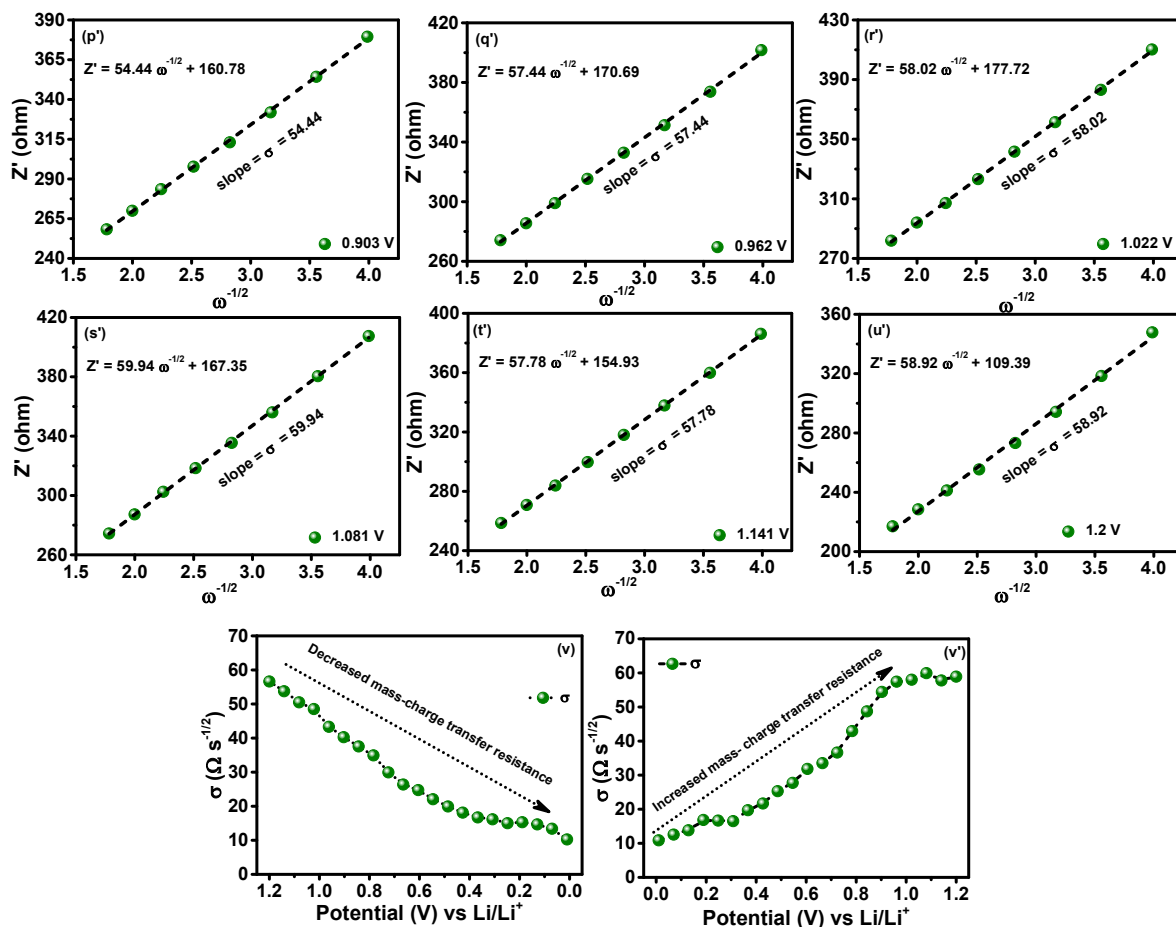


**Figure S16.** Warburg plots, deduced from low frequency portion of DEIS spectra (Figure S14c,d) on MAD600 post 300 cyclic study, for lithiation (a-u) and delithiation (a'-u'). Variation of Warburg coefficient with respect to the potential associated with lithiation (V) and delithiation (V') which were obtained from slope of respective Warburg plots.

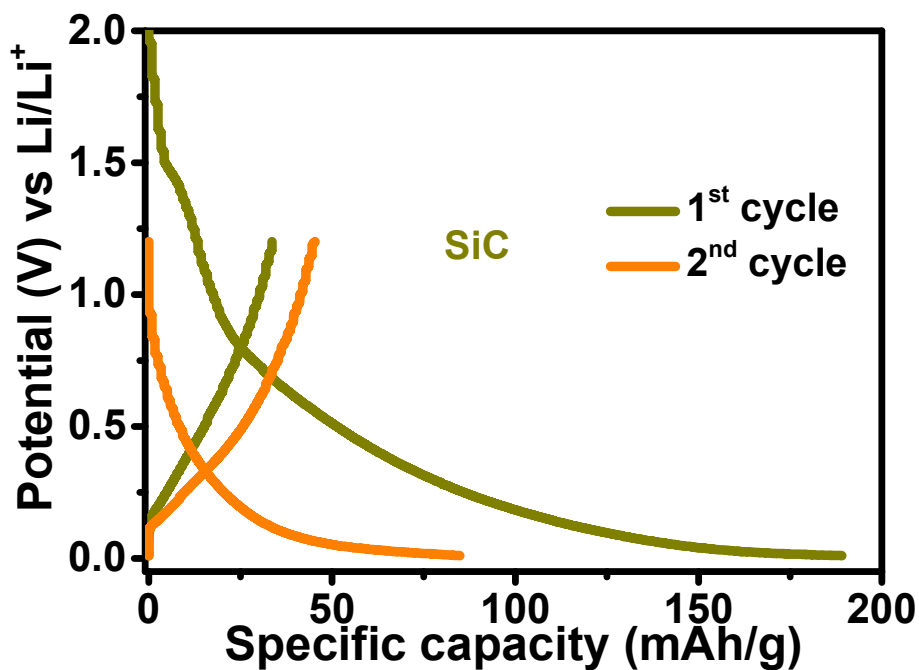


Figure S17. Lithiation-delithiation voltage profiles for first two cycles at 50 mA/g on commercial SiC anode.

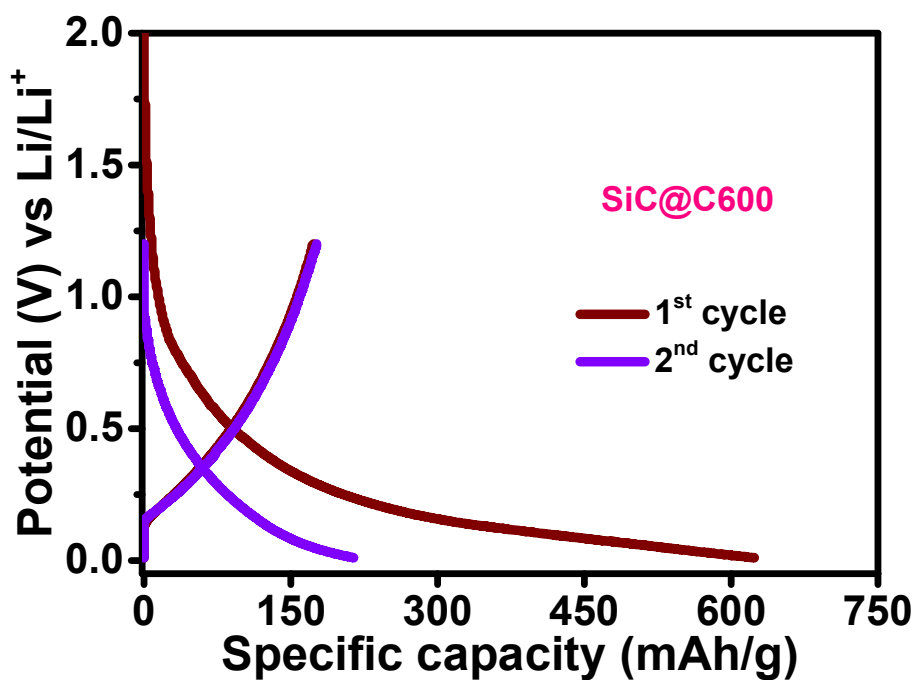
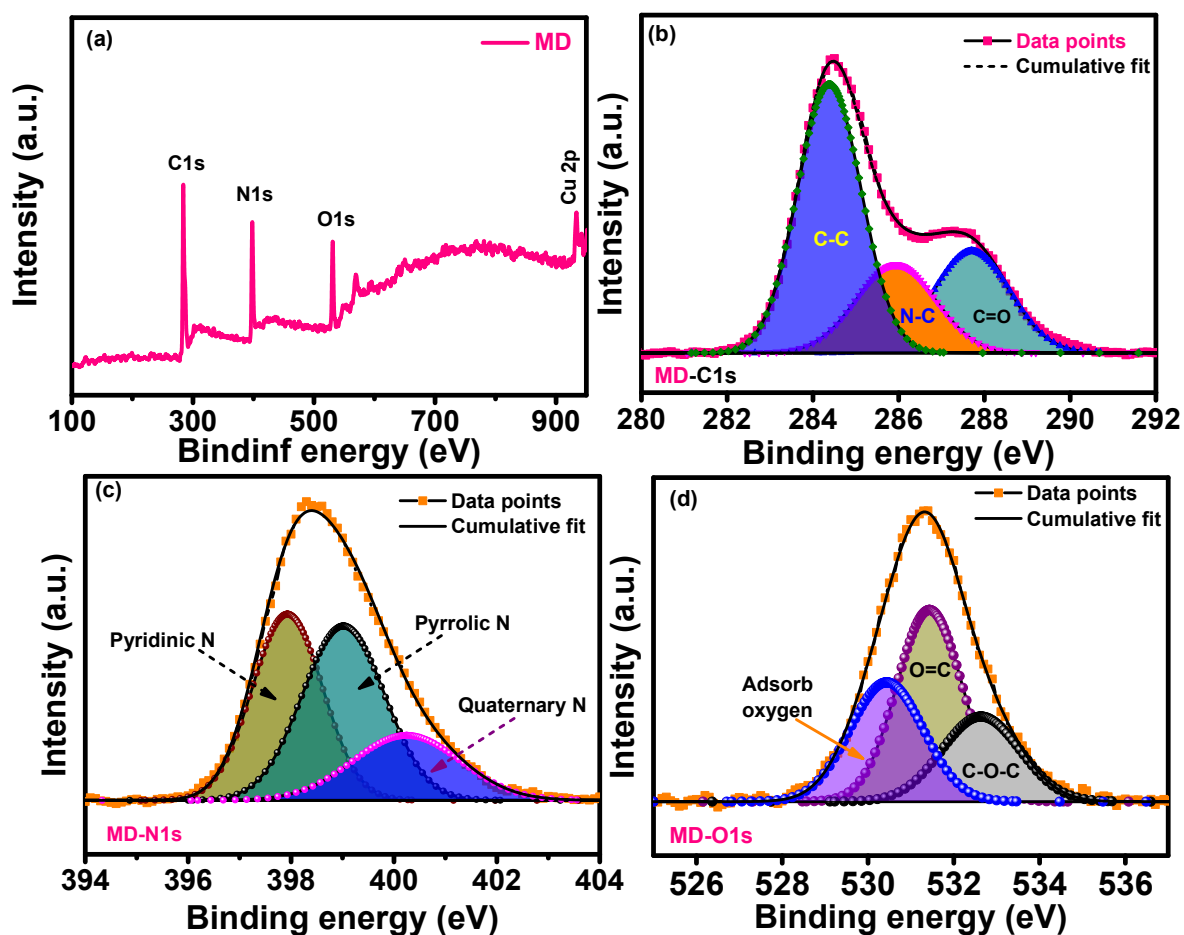
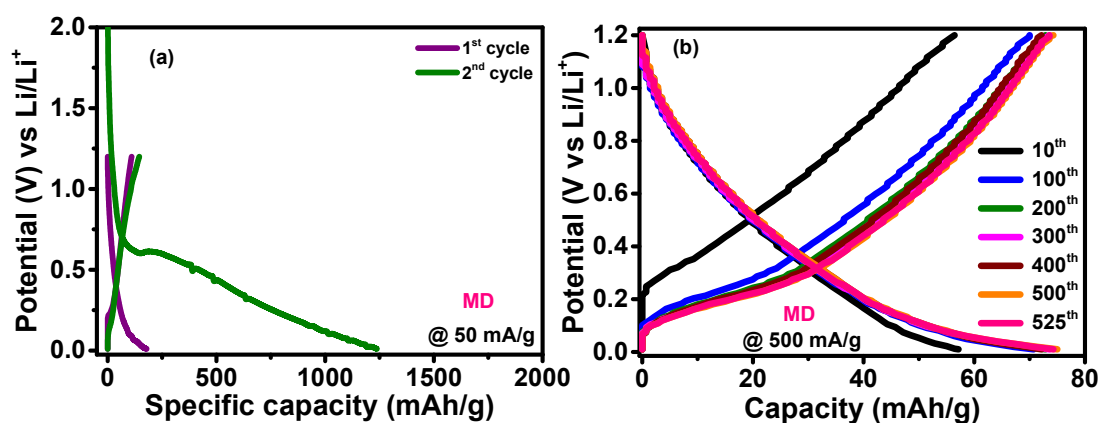


Figure S18. Lithiation-delithiation profiles for first two cycles at 50 mA/g on SiC@C600 anode.



**Figure S19.** (a) Wide XPS spectrum and deconvoluted high resolution core XPS spectra of (b) C1s, (c) N1s and (d) O1s for MD material.



**Figure S20.** Lithiation-delithiation voltage profiles for (a) first two cycles at 50 mA/g, and (b) subsequently selected profiles at 500 mA/g on MD-based anodic half-cell.

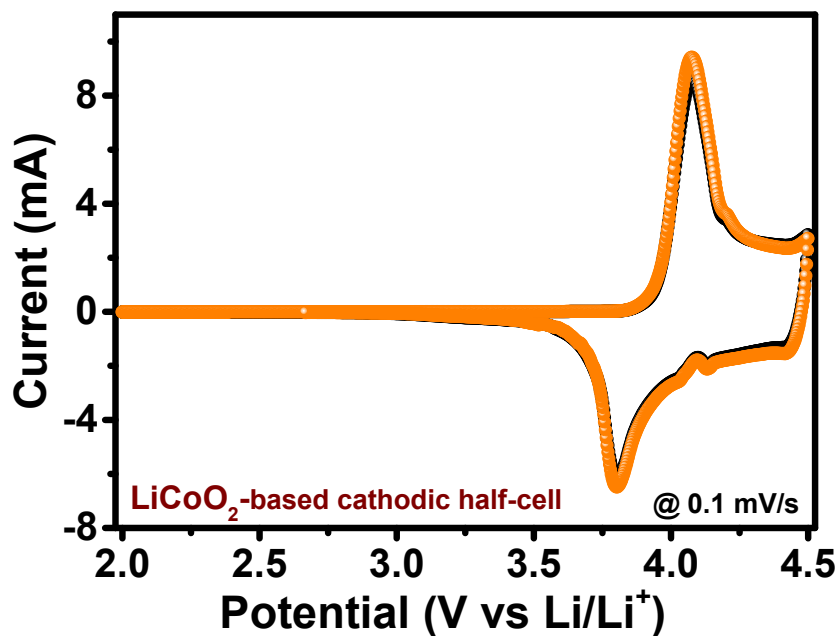


**Figure S21.** Cyclic voltammograms (CV) on commercial  $\text{LiCoO}_2$  based cathodic half-cell.

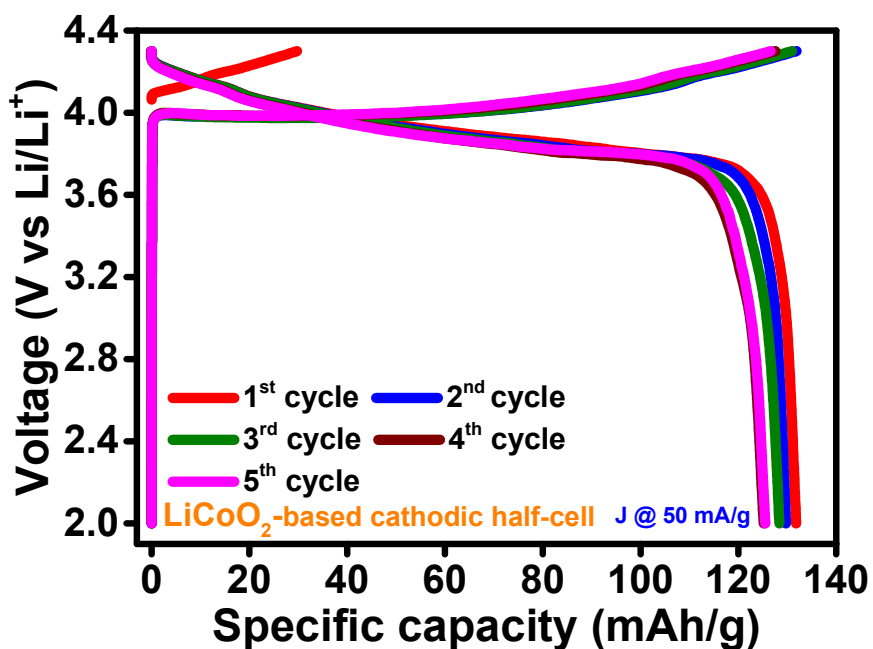


**Figure S22.** Voltage profiles for first five cycles at 50 mA/g on commercial  $\text{LiCoO}_2$  based cathodic half-cell.

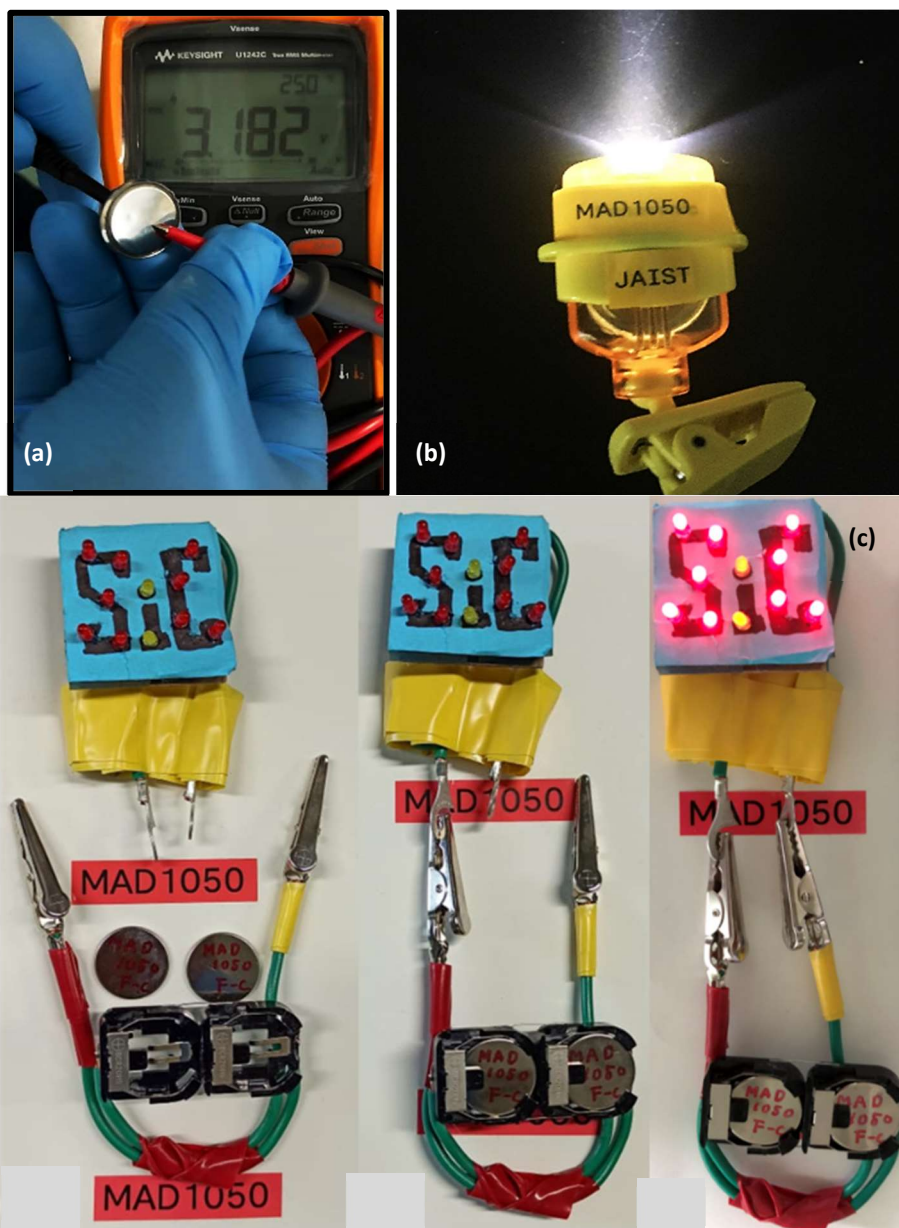


**Figure S23.** (a) A full cell with OCV of  $\sim 3.2$  V and (b,c) a white LED based torch and a LEDs based arrangement powered by  $\text{LiCoO}_2// \text{MAD1050}$  based full cells.



## References

1. J. Wang, D. X. Ye, G. H. Liang, J. Chang, J. L. Kong and J. Y. Chen, *J. Mater. Chem. B*, 2014, **2**, 4338–4345.
2. H. Lee, S. M. Dellatore, W. M. Miller and P. B. Messersmith, *Science (80-. )*, 2007, **318**, 426–430.
3. R. Nandan, H. R. Devi, R. Kumar, A. K. Singh, C. Srivastava and K. K. Nanda, *ACS Appl. Mater. Interfaces*, 2020, **12**, 36026–36039; R. Nandan, A. Gautam, S. Tripathi and K. K. Nanda, *J. Mater. Chem. A*, 2018, **6**, 8537–8548.
4. R. Nandan, P. Pandey, A. Gautam, O. Y. Bisen, K. Chattopadhyay, M. M. Titirici and K. K. Nanda, *ACS Appl. Mater. Interfaces*, 2021, **13**, 3771–3781; R. Nandan, A. Gautam and K. K. Nanda, *J. Mater. Chem. A*, 2017, **5**, 20252–20262.
5. A. Baasner, F. Reuter, M. Seidel, A. Krause, E. Pflug, P. Härtel, S. Dörfler, T. Abendroth, H. Althues and S. Kaskel, *J. Electrochem. Soc.*, 2020, **167**, 020516
6. C. Sun, Y. J. Wang, H. Gu, H. Fan, G. Yang, A. Ignaszak, X. Tang, D. Liu and J. Zhang, *Nano Energy*, 2020, **77**, 105092.
7. H. R. Devi, R. Nandan and K. K. Nanda, *ACS Appl. Mater. Interfaces*, 2020, **12**,

13888–13895.

8. C. Sun, Y. J. Wang, H. Gu, H. Fan, G. Yang, A. Ignaszak, X. Tang, D. Liu and J. Zhang, *Nano Energy*, 2020, **77**, 105092